energies

Article

Energy Harvesting in the Crane-Hoisting Mechanism

Tomasz Haniszewski * and Maria Cieśla

Faculty of Transport and Aviation Engineering, Silesian University of Technology, Krasińskiego 8 Street, 40-019 Katowice, Poland
* Correspondence: tomasz.haniszewski@polsl.pl

Abstract: The subject of the model research contained in this paper is an application of a motion energy–harvesting device on a crane-hoisting mechanism to power independent measurement devices. Numerical experiments focused on the selected motion energy–harvesting device (M-EHS) and its configuration properties in the context of energy-harvesting efficiency in the case of using it on a crane. The results of the computer simulations were limited to the initial specified conditions for the harvester and the movement of the conditions of the crane-hoisting mechanism. The article compares the energy efficiency for the selected construction and parameters of the harvester for specific hoisting speed and the arm length of the motion conversion system. For this purpose, the initial conditions for the crane and the configuration of parameters of the energy harvester were assumed. The results are visualized on the diagram of RMS voltage induced on piezoelectric elements, showing the impact of individual solutions of the proposed motion energy–harvesting device on the efficiency of energy harvesting. The results of the efficiency of the simulations show that the motion harvester ranges from 0.44 V to 14.22 V, depending on the speed of the crane-hoisting mechanism and the length of the arm of the motion conversion system. Still, the design allows for an adjustment to the given conditions by tuning up the M-EHS to a specified excitation frequency and working conditions.

Keywords: crane; hoisting mechanism; nonlinear dynamics; energy harvesting; energy efficiency; M-EHS

Citation: Haniszewski, T.; Cieśla, M. Energy Harvesting in the Crane-Hoisting Mechanism. *Energies* **2022**, *15*, 9366. https://doi.org/10.3390/en15249366

Academic Editors: Wael A. Altabey and Sallam A. Kouritem

Received: 18 November 2022
Accepted: 8 December 2022
Published: 10 December 2022

1. Introduction

Energy harvesting (EH), supplying freely available energy, arouses a lot of interest and attracts the attention of many constructors and designers, especially in the IoT (Internet of Things) systems industry. The predictions about the global use of energy are alarming. According to the IAE report [1] and further research [2], it is modeled that the projected average energy intensity will improve by 2.2% per year by 2030. Therefore, any work with rational and efficient energy consumption is very much desired.

The perspective of collecting energy from the environment seems intriguing. In many applications, it allows the elimination of an external power source, thus simplifying the design of the device and its subsequent operation. Energy harvesting is the result of progress in the field of materials and technologies that enable energy recovery from the background from different sources, yet omitted [3]. The reason for this was the low efficiency of energy conversion and the high cost of manufacturing the devices necessary for this purpose, namely the harvesters. Decreasing the energy consumption of microsystems is also of key importance, which means that energy sources with a power of milliwatts and even microwatts are of practical importance and allow the elimination of traditional power systems using cable systems, batteries, or accumulators of hazardous environmental effects [4].

At the current stage of development of this technology, it is possible to collect energy from many sources, such as electromagnetic radiation, light, heat, or vibration motion, and then convert it into electricity [5].

The area of interest of this manuscript is the kinetic energy of vibrations occurring in the environment of the system, which can be used as a source of electrical energy. Mechanical energy harvesting (MEH) can be obtained from human motion [6,7], fluids [8,9], rotating machines [10,11], and many other sources. The most recent studies on MEH in the transport industry involve road systems: vehicle motion [12], automotive suspension system [13], rotating energy [14,15] as well as railway systems [16] and their elements (such as railroads [17,18] or railway bridges [19]) or handling equipment (such as elevators [20]), harbor electrical cranes [21], gantry cranes [22], and conveyors [23]. The ability to obtain energy is becoming a viable way to increase the energy available in vehicles of various modes of transport.

The main methods for the conversion of the kinetic energy of vibrations are distinguished: electromagnetic, magnetostrictive, electrostatic, triboelectric, and piezoelectric methods [24].

The electromagnetic method uses the phenomenon of electromagnetic induction and the Villari effect, or the inverse of the magnetostriction phenomenon. This effect consists of changing the magnetic parameters of a ferromagnetic because of its deformation [25,26]. As a result, the mechanical energy of vibration is converted into magnetic field energy, which is then converted into electrical energy. Magnetostrictive materials convert magnetic energy into elastic deformation energy [27]. The electrostatic method [28] requires the use of electrets, i.e., materials with permanent dipole polarization, which are the electrical equivalent of permanent magnets [29]. Vibrations are transferred to the surface of the electret, causing the generation of a charge through the triboelectric effect, which is the phenomenon of generating an electric charge through friction or the deformation of materials with electrostatic properties.

Piezoelectric energy harvesting [30–32], shown in the research part of this manuscript, uses the piezoelectric effect. Electric charges appear on the surface of some types of materials (crystals, ceramics, composites, polymers, and bioinspired materials) under the influence of mechanical stress. These stresses can be generated by vibrations propagating in the environment, resulting in the direct conversion of mechanical energy into electrical energy. Researchers work on techniques to increase efficiency for piezoelectric energy harvesting through a nonlinear method [33–36], piezoelectric frequency upconverting [37–39], double pendulum system [40,41], circuit management [42,43], and others.

The energy recovery systems based on the piezoelectric effect are widely described in the literature [36,44–46]. Most of the proposed solutions are based on a kind of vibrating beam—a resonance system with one or several degrees of freedom, in the form of both linear and nonlinear systems [47–50], with particular emphasis on nonlinearity aimed at improving efficiency and applying to a wider spectrum of excitations. Linear systems in the form of a simple vibrating beam are characterized by significant limitations because they have only one resonant frequency, which limits their range of applicability. Most often, nonlinearities aimed at changing these undesirable properties are obtained by adding different configurations of magnetic systems in the form of permanent magnet systems or applied systems based on magnetic induction. The use of the aforementioned magnetic systems causes the system to go into a wider range of resonance frequencies, thus increasing efficiency in a wider frequency spectrum to force the vibration signal. Typically, when applied to self-powered systems such as sensors based on IoT technology, magnetic systems are used that give the mechanical system the character of multistable operation, i.e., bistable and multistable systems, allowing for a wide range of their applicability because of different behaviors in a wide range frequency of extortion. These systems have been extensively described and tested in the literature [51–54].

In this study, the dynamics of the nonlinear bistable vibration acquisition system were investigated. This system is characterized by the work with two stable states, which were forced by the specific configuration of the magnetic system in the tested system. Because the analysis of the behavior of such strongly nonlinear systems is complicated, numerical simulations, which are presented in the following chapters, turned out to be necessary. The parameter values should be taken into careful consideration because in a nonlinear system, even a small change in their value can lead to changes in the behavior of the system, which is a positive feature in the case of parameter control and forcing a specific behavior of the vibrating system. To conclude, the article considered a two-well potential system based on a vibrating beam with attached piezoelectric plates in a system with a motion converter in the form of a classic crosshead crank mechanism with the possibility of using it on an overhead crane (bottom pulley). Therefore, the test system can be modeled as an elastic beam that is subjected to an initial elastic deformation by introducing the housing base into motion, utilizing a rotary to reciprocate the motion converter. Two permanent magnets are attached to the housing and one at the end of the vibrating beam, which enables bistable operation. The second model to be made is the crane-hoisting mechanism model to relate the operation of the energy-harvesting system to the movement of the crane load.

The main research goal of this paper is to formulate a mathematical model and conduct simulations for a new energy-harvesting device based on a vibrating beam on a crane-hoisting mechanism with a motion transformation system for powering an independent measurement device allowing energy harvesting.

This manuscript is organized as follows. Section 1 includes the introduction and review of the scientific literature of the manuscript and outlines previous research on electromechanical energy harvesting and the methods applied. Section 2 describes the research approach and specifies the methodology. It presents mathematical models focused on the selected energy-harvesting device and its configuration properties in the context of energy-harvesting efficiency and its cooperation with the hoisting mechanism of a crane. Section 3 outlines the results of computer simulations limited to specified initial conditions for the crane-hoisting mechanism. Section 4 presents a discussion of the results obtained during the analysis performed. The results are visualized with the RMS voltage diagram induced on piezoelectric elements, a bifurcation diagram, and phase portraits, showing the impact of the individual control parameter configuration on the proposed motion energy–harvesting device on the efficiency of energy harvesting. Finally, Section 5 is devoted to summary and conclusions.

2. Mathematical Model Formulation

The basis for presenting the numerical models necessary to research energy production is a single-girder overhead traveling crane equipped with a double-pin gripper. This crane has a load capacity of 5 t and a girder span of 20 m, where the maximum lifting height is 10 m.

The structure under consideration comprises a trolley. In the drive system of the tested hoisting mechanism, a 10 kW asynchronous motor was used. The rope system used is a typical four-rope solution for overhead cranes with a double pulley system and a total ratio of 2 (Figure 1). The characteristics of the hoisting mechanism are presented in Table 1.

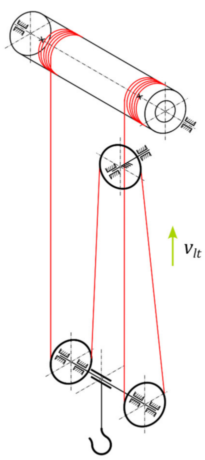

Figure 1. Installed rigging system with equalizing pulley.

Table 1. Characteristics of the hoisting mechanism.

Name	Symbol	Unit	Value
lifting capacity	Q	kg	5000
lifting speed	v_{lt}	ms^{-1}	0.208
lifting height	$H_{lt(\max)}$	m	10
motor *SZUDe* 56*b*	P_{rd}	kW	10
	ω_{rd}	$\mathrm{rad{\cdot}s^{-1}}$	98.96
gear ratio	i_{gr}	–	60
rope drum diameter	D_{dm}	m	0.5
wire rope type		$SEALE\ 6 \times 19 + FC\ sZ$	
wire rope diameter	d_{re}	m	0.012
number of strands of rope	n_{re}	–	4
drum rotation	ω_{dm}	$\mathrm{rad{\cdot}s^{-1}}$	~1.65

2.1. Model of the Overhead Crane-Hoisting Mechanism with the Simplified Drive System

Nowadays, in crane construction, the most common drives use electric asynchronous motors. This drive does not create significant limitations on the lifting capacity or speed of the working movements, which can achieve the required efficiency of lifting machines. Because of the easy access to alternating current in crane drive systems, asynchronous motors have found wide applications.

$$
\begin{gathered}
\frac{d}{dt} M_n = \left(\Omega_s - p\frac{d}{dt}\varphi_{1n}\right)\Theta - T_e^{-1} M_n \\
\frac{d}{dt}\Theta = -\left(\Omega_s - p\frac{d}{dt}\varphi_{1n}\right) M_e + 2T_e^{-1} M_k - T_e^{-1} \\
\frac{d}{dt}\varphi_{1n} = J_w^{-1}(M_n - M_0)
\end{gathered} \tag{1}
$$

where M_n represents motor torque, $\frac{d}{dt}\varphi_{1n}$ represents angular velocity of the rotor, Θ represents an auxiliary variable having the physical dimension of the moment, $T_e = \Omega_s^{-1} s_k^{-1}$—represents time constant, and M_0 represents the moment of resistance.

Many numerical models of electric motors have been described in the literature; this article uses one of the simpler dynamic models of an asynchronous motor [55]. The tested hoisting mechanism was equipped with a SZUDe 56b ring hoist motor. On the basis of the catalog data, the parameters of the motor necessary for the numerical experiment are described in Table 2. Thus, the excitation model takes the form of a system of a three-differential equation, Equation (1). Physical parameters are presented in Table 2.

Table 2. Parameters of the modeled asynchronous motor.

Symbol	Name	Value	Unit
P_{zn}	rated power	10×10^3	W
γ_s	overload	320	%
J_w	moment of inertia of the rotor	0.1425	kgm^2
M_k	maximum, critical moment	323.36	Nm
M_{nom}	nominal moment	101.05	Nm
n_{zn}	speed-rated rotor	945	rpm
n_s	synchronous speed	1000	rpm
s_n	nominal slip	0.055	–
s_k	critical slip	0.343	–
ω_{zn}	rated angular speed of the motor	98.96	$\mathrm{rad{\cdot}s^{-1}}$
Ω_s	circular frequency of the supply network	314.15	$\mathrm{rad{\cdot}s^{-1}}$
ω_o	synchronous angular speed of the motor	104.72	$\mathrm{rad{\cdot}s^{-1}}$
P	number of pole pairs	3	–
f_z	mains frequency	50	Hz

One of the main components of the hoisting mechanism is the drive system. The excitation task is essential here because of its impact on the acceleration values of individual elements of the system. The values of the drive torque and the energy supplied to the system in an amount that can achieve the intended lifting speed and start-up time are critical here. To implement the motor model (1), the reduced drive system of the hoisting mechanism presented in Figure 2 was considered. The model includes the motor, the coupling with the motor shaft, the reduced gear transmission representing the speed reduction system, and the cable drum. The inertia of the rotating parts was combined with elastic and damping elements with linear characteristics.

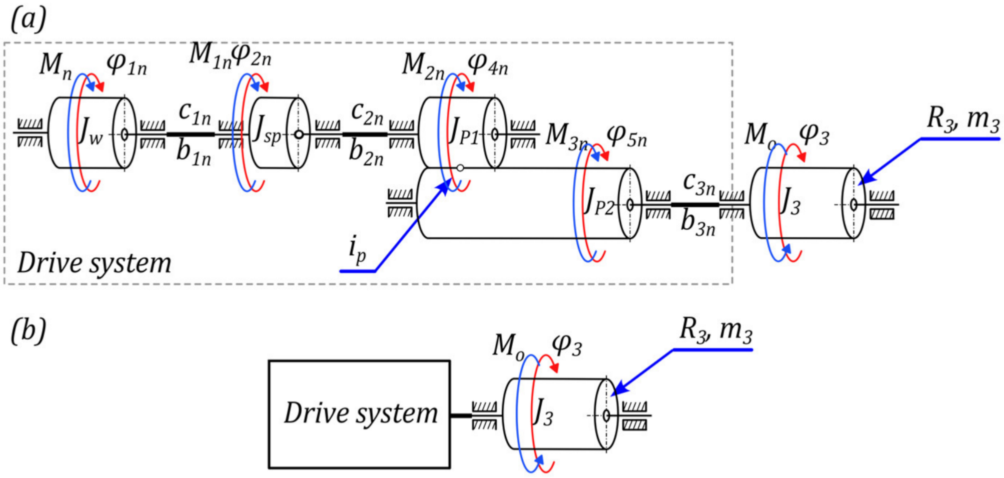

Figure 2. Simplified drive system: (**a**) base model and (**b**) simplified diagram.

Given the proposed motor model and the reduced drive mechanism (Figure 2), the system of the six-differential equation, Equation (2), is finally obtained:

$$
\begin{aligned}
J_w \frac{d^2\varphi_{1n}}{dt^2} &= M_n + c_{1n}(\varphi_{2n} - \varphi_{1n}) + b_{1n}\left(\frac{d\varphi_{2n}}{dt} - \frac{d\varphi_{1n}}{dt}\right) \\
\frac{dM_n}{dt} &= \left(\Omega_s - p\frac{d\varphi_{1n}}{dt}\right)\Theta - T_e^{-1}M_n \\
\frac{d\Theta}{dt} &= -\left(\Omega_s - p\frac{d\varphi_{1n}}{dt}\right)M_n + 2T_e^{-1}M_k - T_e^{-1} \\
J_{sp}\frac{d^2\varphi_{2n}}{dt^2} &= -c_{1n}(\varphi_{2n} - \varphi_{1n}) + c_{2n}(\varphi_{4n} - \varphi_{2n}) - b_{1n}\left(\frac{d\varphi_{2n}}{dt} - \frac{d\varphi_{1n}}{dt}\right) + b_{2n}\left(\frac{d\varphi_{4n}}{dt} - \frac{d\varphi_{2n}}{dt}\right) \\
\left(J_{p1} + \frac{J_{p2}}{i_p^2}\right)\frac{d^2\varphi_{4n}}{dt^2} &= -c_{2n}(\varphi_{4n} - \varphi_{2n}) + c_{3n}i_p^{-1}\left(\varphi_3 - \varphi_{4n}i_p^{-1}\right) - b_{2n}\left(\frac{d\varphi_{4n}}{dt} - \frac{d\varphi_{2n}}{dt}\right) + b_{3n}i_p^{-1}\left(\frac{d\varphi_3}{dt} - \frac{d\varphi_{4n}}{dt}i_p^{-1}\right) \\
J_3\frac{d^2\varphi_3}{dt^2} &= (-\Xi_1 R_3 - \Xi_{1p}R_3) - c_{3n}\left(\varphi_3 - \varphi_{4n}i_p^{-1}\right) - b_{3n}\left(\frac{d\varphi_3}{dt} - \frac{d\varphi_{4n}}{dt}i_p^{-1}\right)
\end{aligned}
\tag{2}
$$

Because the mesh stiffness of the gear wheels is represented by the inertial elements J_{p1} and J_{p2} is not taken into account, the values of the rotation angles can be described as follows:

$$\varphi_{5n} = \varphi_{4n}i_p^{-1};\ \frac{d\varphi_{5n}}{dt} = \frac{d\varphi_{4n}}{dt}i_p^{-1} \tag{3}$$

The last and at the same time main element of the complete model of the hoisting mechanism is the rope system (with rope stiffness shown in Figure 3) with the load and the reduced girder of the tested crane. The structure of the proposed phenomenological model makes it possible to carry out numerical simulations of the discussed system for different lengths of ropes, and the described model of the drive system makes it possible to set a specific start-up curve described by a set in Equation (4) (Figure 4). The model presented in Figure 5 allows numerical simulations of the operation of the crane-hoisting mechanism. The physical parameters describing the drive system model are shown in Table 3. Because of the stiffness of the variable value of the wire rope depending on its length, each of the proposed models included a rope drum and the ground, thus imitating the shortening of the rope during the hoisting process.

$$(a)\begin{cases} t < t_p,\ A = 0 \\ t \le (t_p + t_n),\ A = 0.5A_n\left(1 - \cos\left(\pi t_n^{-1}(t - t_p)\right)\right) \\ t \ge (t_p + t_n),\ A = A_n \end{cases} \quad (\mathrm{b})\begin{cases} t < t_p,\ A = 0 \\ t \ge t_p,\ \ A = A_n \end{cases} \tag{4}$$

where A represents amplitude, A_n represents nominal amplitude, t_n represents rise time, and t_p represents delay.

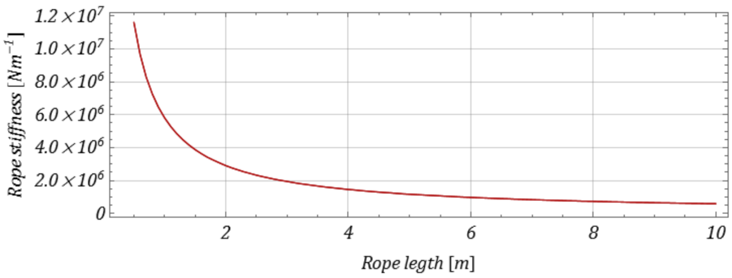

Figure 3. Rope stiffness for E_l = 0.5E_s (metallic rope cross section).

Table 3. Physical parameters describing the model of the drive system.

Symbol	Name	Value	Unit
J_w	mass moment of inertia of the motor rotor	0.1425	kgm^2
J_{sp}	mass moment of inertia of the clutch	0.1634	kgm^2
J_3	mass moment of inertia of the rope drum	11.1647	kgm^2
J_{p1}	mass moment of inertia of the input stage of the substitute gear	0.057	kgm^2
J_{p2}	mass moment of inertia of the output stage of the substitute gear	0.635	kgm^2
c_{1n}	the stiffness of the shaft connecting the motor to the clutch	2.05×10^5	Nm·rad^{-1}
c_{2n}	the stiffness of the shaft connecting the clutch to the gear	5.58×10^4	Nm·rad^{-1}
c_{3n}	the stiffness of the shaft connecting the gears to the rope drum	4.92×10^6	Nm·rad^{-1}
b_{1n}	damping of the shaft connecting the motor with the clutch	1.02×10^3	Nms·rad^{-1}
b_{2n}	damping of the shaft connecting the clutch with the gear	2.79×10^2	Nms·rad^{-1}
b_{3n}	damping of the shaft connecting the gears with the rope drum	2.46×10^4	Nms·rad^{-1}

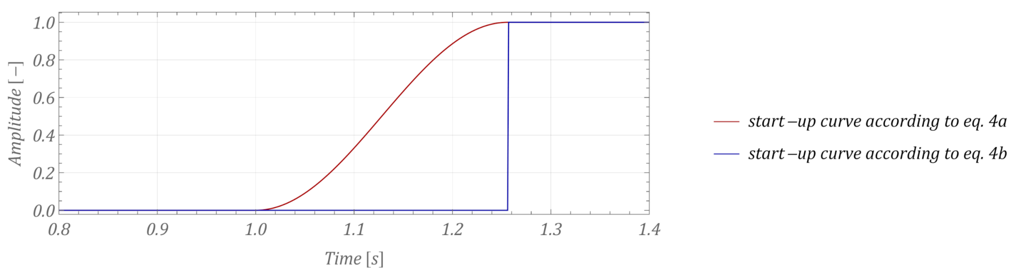

Figure 4. Sample excitation profiles.

Figure 4 shows the excitation curves for an exemplary delay time of 1 second and an increase time of 1.257 s. For presenting the curves, the torque value was replaced with a dimensionless amplitude. Figure 5 presents the physical model of the hoisting mechanism together with a simplified girder, represented by a beam described by elastic and damping parameters c_1, b_1.

$$
\begin{aligned}
m_1 \frac{d^2 q_1}{dt^2} &= -c_1 q_1 - b_1 \frac{dq_1}{dt} - c_3(q_1 - q_3) + \left(\Xi_2 + \Xi_{2p}\right) \\
m_2 \frac{d^2 q_2}{dt^2} &= -F_{dp} - m_2 g + c_2(-q_2 + q_4) \\
m_3 \frac{d^2 q_3}{dt^2} &= c_3(q_1 - q_3) + \left(\Xi_1 + \Xi_{1p}\right) \\
m_4 \frac{d^2 q_4}{dt^2} &= \left(\Xi_1 + \Xi_{1p}\right) + \left(\Xi_2 + \Xi_{2p}\right) - c_2(-q_2 + q_4) \\
J_4 \frac{d^2 \varphi_4}{dt^2} &= (\Xi_1 - \Xi_2) R_4 + \left(\Xi_{1p} - \Xi_{2p}\right) R_4
\end{aligned} \tag{5}
$$

$$
\begin{aligned}
\Xi_1 &= c_{l1}(-q_4 - R_4\varphi_4 - q_3 + R_3\varphi_3) \\
\Xi_2 &= c_{l2}(-q_4 + R_4\varphi_4 - q_1) \\
\Xi_{1p} &= b_{l1}\left(-\frac{dq_4}{dt} - R_4\frac{d\varphi_4}{dt} - \frac{dq_3}{dt} + R_3\frac{d\varphi_3}{dt}\right) \\
\Xi_{2p} &= b_{l2}\left(-\frac{dq_4}{dt} + R_4\frac{d\varphi_4}{dt} - \frac{dq_1}{dt}\right)
\end{aligned} \tag{6}
$$

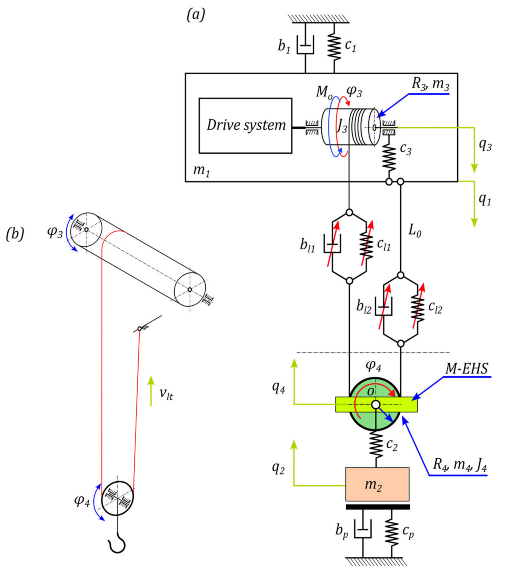

Figure 5. (**a**) An extended model of the hoisting system with the drive system and (**b**) a simplified rigging system without equalizing the pulley.

The model includes the reduced mass of the girder together with the mass of the cable drum, the mass of the trolley, and the load. The wire rope is represented in the form of a Kelvin–Voight model, where the stiffness and damping depend on the length of the rope and its mass in the case of damping. The model also considers a double-rope strand, the flexibility of the rope drum axle bearings, and the bottom block in the form of a bottom pulley with a radius of R_4. It was assumed that the deformations of the elastic elements represent the stiffness of the load-carrying structure, the bearings of the rope drum axis, and the ground, which are small and linearly dependent on the forces, and that at low speeds, the resistance force of the viscous damper used is directly proportional to the speed. On the basis of the physical models presented in Figures 2 and 5, the system of differential equations of motion (5)–(10) [56] is presented for the wire ropes modeled with the nonlinear Kelvin–Voight model:

Because the system has direct control over the movement of the load through the drive of the cable drum, it is necessary to consider the ground supporting the load in the initial phase of the movement of the masses of the system. The reaction force of the ground

F_{dp} was made dependent on the displacement; at the moment of rest, the force of the elasticity and damping of the ground acts on the load, and when the load is lifted, this force is excluded from the system. The value of the reaction force is described by the relation in Equation (7).

$$F_{dp} = \begin{cases} 0 & q_2 \geq 0 \\ c_p q_2 + b_p \dot{q}_2 & q_2 < 0 \end{cases} \tag{7}$$

On the basis of [55], it was assumed that the average value of Young's modulus for wire ropes with a fiber core is approximately half of the value of Young's modulus for steel.

$$E_l = (0.4 \div 0.65) E_s \approx 0.5 E_s \tag{8}$$

The values of the modulus of elasticity for the ropes are described in Equation (8) and should be used for ropes containing fiber cores. In the case of ropes with a steel core, a modulus value similar to Young's modulus of the material from which the rope is made should be used for calculation purposes. According to Costello [57], within (0.9–1) is Young's modulus for steel. The model considers the dynamic forces occurring in the rope, broken down into elastic and damping forces, where the stiffness of the ropes is described by the relationship, in Equation (9), and the value of the stiffness n_l of the strands depends on its length, where the variable damping coefficient of the rope strand is defined by the dependence, in Equation (10).

$$\begin{gathered} c_{l1} = \varsigma \frac{E_l A_l}{(L_0 - R_3 \varphi_3)},\ (L_0 - R_3 \varphi_3) = L_1(t), where\ \varsigma = \frac{n_l}{i_w} \\ c_{l2} = \varsigma \frac{E_l A_l}{(L_0 - i_w R_4 \varphi_4)},\ (L_0 - i_w R_4 \varphi_4) = L_2(t) \end{gathered} \tag{9}$$

$$b_{lj} = 2\zeta \sqrt{c_{lj}\left(0.5 m_2 + \varsigma \rho_l A_l L_j(t)\right)},\ where: j = 1, 2 \tag{10}$$

The parameters of the physical model considered are listed in Table 4.

Table 4. Physical parameters describing the model of the drive system.

Symbol	Name	Value	Unit
m_1	the reduced mass of the girder together with the weight of the winch trolley	5500	kg
m_2	mass of the load	1850	kg
m_3	weight of the rope drum	280	kg
m_4	doubled weight of the pulley, bottom pulley	30	kg
J_4	mass moment of inertia of doubled pulley, bottom pulley	0.3	$kg \cdot m^2$
c_1	girder stiffness	4.6×10^6	N/m
c_p	ground stiffness	2.0×10^8	N/m
c_3	stiffness of the rope drum axle bearings	1.8×10^8	N/m
c_2	hook stiffness	2×10^7	N/m
b_p	ground damping	1×10^6	N·s/m
b_1	Damping of the girder	5.0168×10^3	N·s/m
R_3	radius of the rope drum	0.25	m
R_4	radius of the lower pulley	0.14	m
d_l	rope diameter	0.012	m
L_0	initial rope length	10	m
A_l	metallic cross section of the rope	5.53×10^{-5}	m^2
ρ_L	steel density	7850	$kg \cdot m^{-3}$
E_s	Young's modulus for steel	2.1×10^{11}	Pa
E_l	the modulus of elasticity of the rope	1.05×10^{11}	Pa
g	acceleration due to gravity	9.81	$m \cdot s^{-2}$
v_{lt}	lifting speed	0.208	m/s
ω_b	angular velocity of the rope drum	1.67	rad/s
n_l	number of strands of rope	4	–
ζ	dimensionless damping factor for wire ropes	0.07	–
i_p	transmission ratio	60	–
i_w	transmission of the rope system	2	–

2.2. Model of M-EHS (Motion Energy–Harvesting System)

The subject of the model tests presented in this chapter is a system to obtain energy with a two-well potential barrier described according to the dependence (16). The tested structure consists of two parts, where the first one is a typical system consisting of a flexible cantilever beam II, fixed in a nondeformable body V, which is fastened with screws to the housing of the object generating mechanical vibrations, which in this case is the base III performing a reciprocating motion. Under the influence of vibrations described in the examined case with the function $q_e(t)$, the flexible beam II is knocked out of the equilibrium position, as a result of which an electric voltage is generated on the electrodes of the piezoelectric I as a result of their deformation. The second part is a system for converting the rotational motion of the lower pulley into a reciprocating motion, which was conducted by using a classic crosshead crank system. The article does not discuss the construction or influence of the masses of individual structural elements of the motion converter system.

In the M-EHS, a linear mechanical characteristic of the beam was assumed, and the nonlinearities in the tested system were mapped because of the interaction between the permanent magnets fixed to the housing V and the movable magnet placed on the beam II. In addition, the dissipating element factors in the energy losses caused by deformation and friction at the point of attachment to a rigid, nondeformable V frame. Two permanent magnets are permanently symmetrically placed in the frame, interacting with a moving magnet at the end of the beam. The distance between the set of permanent magnets and the moving magnet was discussed in [58–61].

$$\begin{array}{c} \frac{d^2q_h}{dt^2} + 2h_h\frac{dq_h}{dt} + \omega_{0h}^2 q_h + \sigma_e u + \chi = 2h_h\frac{dq_e}{dt} + \omega_{0h}^2 q_e \\ \frac{du}{dt} + u\psi - \mu\left(\frac{dq_h}{dt} - \frac{dq_e}{dt}\right) = 0 \end{array} \tag{11}$$

where $\frac{c_h}{m_h} = \omega_{0h}^2, \frac{b_h}{m_h} = 2h_h, \sigma = \frac{k_p}{m_h},\ \psi = \frac{1}{C_P R_Z},\ \mu = \frac{k_P}{C_P},\ \chi = \frac{F_m}{m_h}$.

Therefore, the M-EHS under consideration is characterized, compared with other solutions, using a crank and crosshead system to change the rotary motion to reciprocating, thus giving the possibility of using it directly on the lower pulley of the crane-hoisting mechanism. On the basis of the formulated phenomenological model, differential equations of motion, in Equation (11), were derived, constituting a formal basis for conducting quantitative and qualitative numerical experiments, where the excitation functions were presented in the form of Equation (12). To increase the excitation frequency, a gear in the form of an additional wheel with a radius of R_5 cooperating with the pulley of the lower block and at the same time increasing the value of the angular velocity by $R_4R_5^{-1}$ was assumed:

$$\begin{array}{c} q_e = R_5\left(1 - cos\varphi_5 + 0.5R_5 l_e^{-1}\sin^2\varphi_5\right) \\ \frac{dq_e}{dt} = R_5\frac{d\varphi_5}{dt}\left(sin\varphi_5 + 0.5R_5 l_e^{-1}\sin(2\varphi_5)\right) \end{array} \tag{12}$$

where $\varphi_5 = \varphi_4 i_{wh} = (\omega_w t)R_4R_5^{-1},\ \frac{d\varphi_5}{dt} = \omega_w R_4 R_5^{-1}$.

In Model (11) m_h represents the mass of the permanent magnet loading the beam (Figure 6), q_h corresponds to the displacement of the mass m_h, and F_m represents the force reflecting the interaction of magmatic forces and the displacement of the beam.

$$F_m = c_{h1}x + c_{h2}x^3 + c_{h3}x^5 \tag{13}$$

In the case of numerical calculations, the function representing the interactions between the magnets is described as a polynomial function of the nth order [36,62]. In the case under study, it was assumed that it would be a polynomial of order 5 (13). The formal basis for computer simulations is a nonlinear differential equation, Equation (14). For this purpose, a new variable was introduced, defined as the difference of displacements $x = (q_h - q_e)$:

$$\begin{array}{c} \frac{d^2x}{dt^2} + 2h_h\frac{dx}{dt} + \omega_{0h}^2 x + \sigma_e u + \chi = \frac{d^2q_e}{dt^2} \\ \frac{du}{dt} + u\psi - \mu\frac{dx}{dt} = 0 \end{array} \tag{14}$$

where $\frac{d^2q_e}{dt^2} = R_5\omega_w^2 i_{wh}^2 \left(cos((\omega_w t)i_{wh}) + R_5 l_e^{-1}\cos(2(\omega_w t)i_{wh})\right)$.

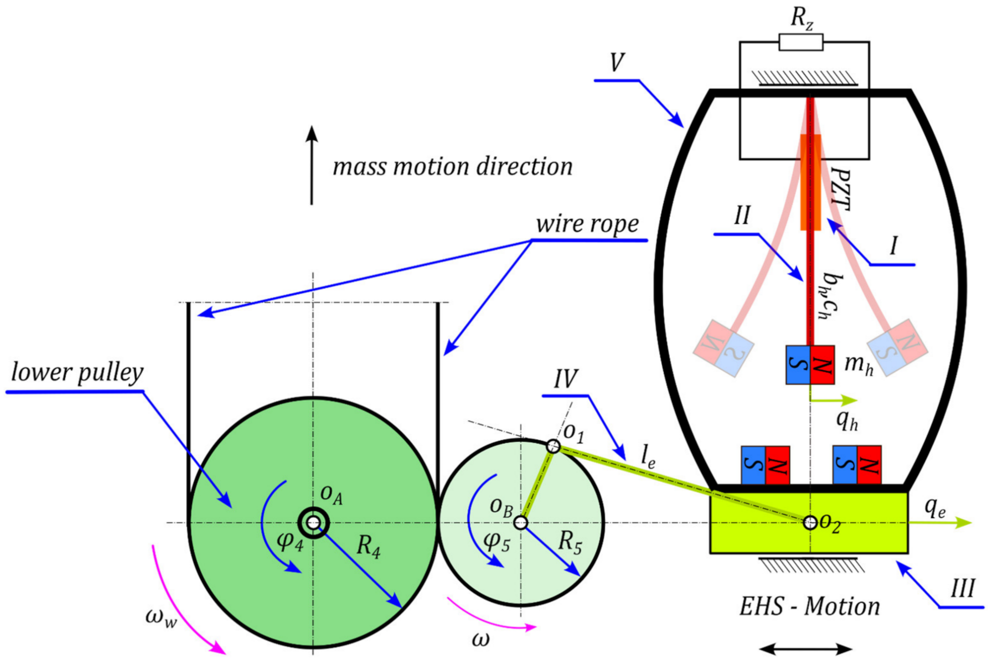

Figure 6. M-EHS (motion energy–harvesting system).

This article presents the results of the numerical calculations of the M-EHS. The coefficients of the polynomial function (13) are presented in Table 5. On this basis, the potential energy function (Figure 7) was defined as follows:

$$E_p = \frac{1}{2}c_h x^2 + \frac{1}{2}c_{h1}x^2 + \frac{1}{4}c_{h2}x^4 + \frac{1}{6}c_{h3}x^6 \tag{15}$$

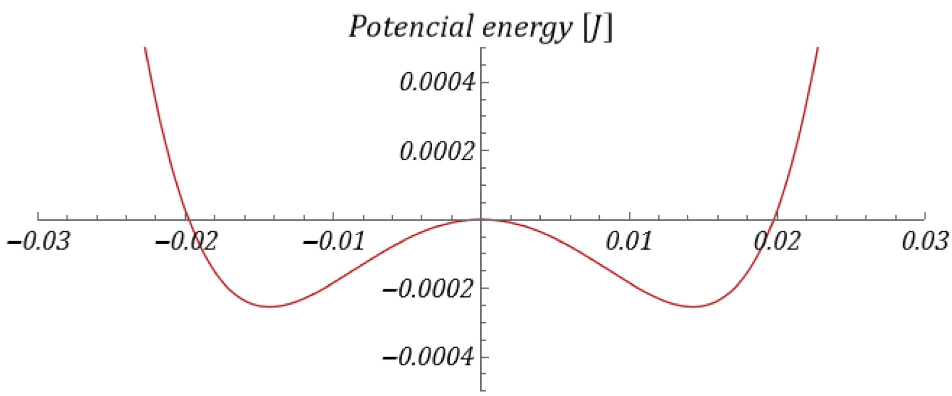

Figure 7. Potential energy functions of M-EHS for a specified magnet position.

Table 5. Geometric and physical parameters of the model.

Name	Symbol	Value	Unit
inertial element (mass) loading the beam	m_h	0.0145	kg
energy losses in a mechanical system	b_h	0.03	Nsm^{-1}
stiffness of beam-pzt system	c_h	2.9	Nm^{-1}
arm length	l_e	$0.01,\ 0.035,\ 0.07$	m
Angular velocity of lower pulley	ω_w	$0.5 - 3.0$	s^{-1}
radius of the wheel cooperating with the lower pulley	R_5	0.014	m
parameters defining the potential barrier	c_{h1}	-7.6	Nm^{-1}
	c_{h2}	1.9×10^5	Nm^{-3}
	c_{h3}	1.94×10^7	Nm^{-5}
ratio	i_{wh}	10	–
equivalent resistance of the electrical circuit	R_Z	1.1×10^6	Ω
equivalent capacity of the electric circuit	C_P	72	nF
electromechanical constant of piezoelectric converter	k_P	3.98×10^{-5}	NV^{-1}

The derived equations of motion, in Equation (14), are the formal basis for carrying out model tests of the considered M-EHS together with the hoisting model described by Equations (5)–(10).

3. Model Test Results

The model tests were divided into two stages: the first includes simulations of the dynamics of the load-hoisting mechanism, and the second concerns the model tests of the M-EHS. Simulations of the dynamic load-hoisting model were performed for the excitation in the form of a step signal forcing the engine to work (Figure 4), assuming loose ropes in the start-up phase (zero initial conditions). The simulation results are presented in Figure 8.

Motor start was performed using the step curve described by relation (b) in Equation (4), which reflects immediate engine start. Figure 8 shows a series of graphs containing data relevant according to the possibility of obtaining energy in the considered mechanism. As can be seen, the sudden start-up and the lack of initial tension in the wire ropes cause a significant increase in the amplitude of the girder vibrations q_1 concerning the static value; thus, the amplitude of the acceleration of the girder center reaches a value of about 2 ms^{-2}. After passing the transient state, the system stabilizes, and the lifting speed $\dot{q}_2$ reaches the nominal value of about 0.2 ms^{-1} and the vibrations of the bridge and the axis of the lower pulley stop after 3 s. The results obtained are typical for cranes, characterized by intermittent motion. However, the use of this type of mechanical vibration with a relatively rapidly decreasing amplitude may turn out to be difficult and unjustified in terms of the hoisting mechanism. Therefore, it is reasonable to use a vibration recovery system in the form of the system shown in Figure 6 based on the rotation of the lower pulley. In the case of the vibrations of both the bridge and the axis of the lower pulley, the voltage generated by the system will be short-lived, and the accumulation of energy in this way may turn out to be ineffective. In the next stage, the crane model will be replaced with a system of equations representing the operation of the lower pulley and by modifying its operating parameters, such as speed and the parameters of the rotary motion converter system to reciprocate; by changing the parameters of the arm length l_e and ω_w, their impact on the efficiency of energy acquisition will be examined using voltage diagrams U_{rms}.

Taking into account the course of the angular velocity of the lower pulley (Figure 8i), it was assumed that the energy acquisition would occur in steady motion; therefore, it is reasonable to use the proposed Equation (12) to reflect the operation of the pulley.

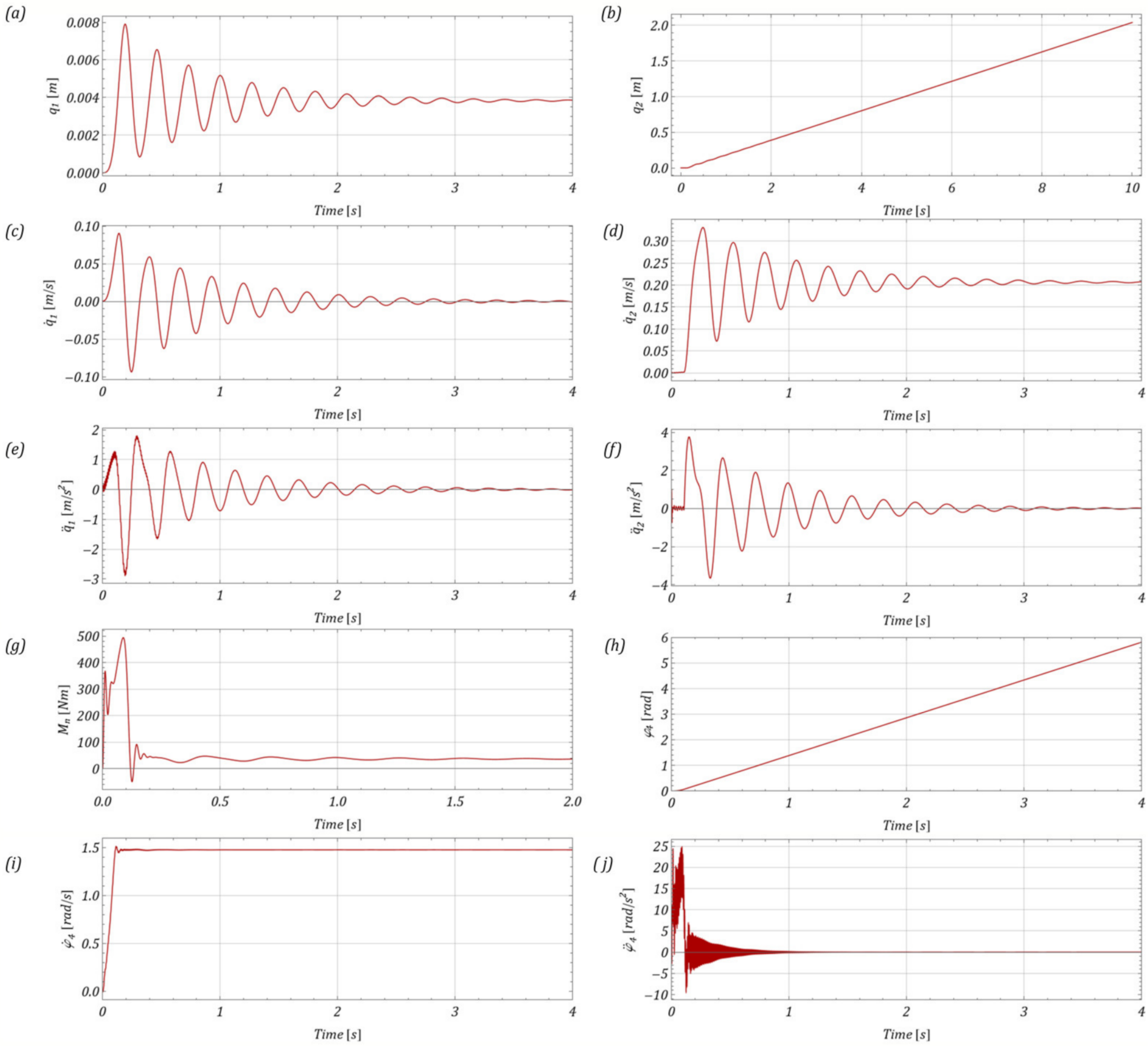

Figure 8. Time series of the dynamic selected variables of the hoisting model, (**a**) crane girder vibration amplitude as a function of time, (**b**) load displacement amplitude as a function of time, (**c**) speed of the crane girder center as a function of time, (**d**) load movement speed as a function of time, (**e**) acceleration of the crane girder center as a function of time, (**f**) acceleration of a moving load as a function of time, (**g**) motor drive torque as a function of time, (**h**) angle of rotation of the lower sheave as a function of time, (**i**) angular velocity of the lower block sheave as a function of time, (**j**) angular acceleration of the lower pulley as a function of time.

4. Model Test Results and Effectiveness of M-EHS for Different Excitation Parameters

Model tests were conducted with the energy acquisition system, for which the energy potential is described by two wells (Figure 7). It was assumed that the system was affected by excitation q_e with amplitude l_e (converter arm) and frequency ω_w (angular velocity of the lower pulley). Model studies were performed with the assumption of the adopted data and phenomenological models included in the article. To determine the dependence influence of the adopted control parameters, l_e (converter arm) and the frequency ω_w (angular velocity of the lower pulley), many tools were used to reveal the impact of the assumed parameters on the efficiency of the energy acquisition of the M-EHS under examination. Some tools were used to reveal the location of both chaotic and periodic zones. For this purpose, two numerical tools were used: bifurcation diagrams and diagrams of the largest Lyapunov exponent [63,64]. Both chaotic zones and zones of periodic solutions are presented in the form of a multicolored map showing the distribution of the maximum Lyapunov exponent (Figure 9).

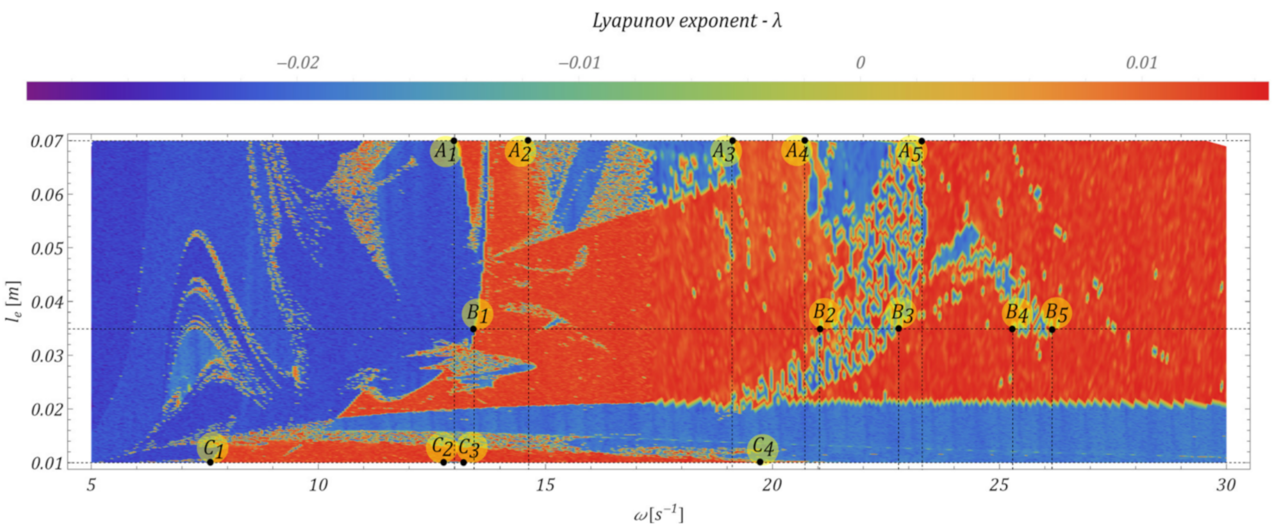

Figure 9. Multicolored map of the largest Lyapunov exponent generated under zero initial conditions, presented in the form of a two-dimensional graph based on arm length (l_e) and frequency (ω).

The map in Figure 9 covers a wide range of frequencies, starting at 5 and ending in 30 s^{-1}, thus presenting the dynamics of the system in a wide spectrum. This approach visually characterizes how motion vibration affects the M-EHS. The two-dimensional map shown in Figure 9 was determined with zero initial conditions: $x(0) = 0$, $\dot{x}(0) = 0$, $u(0) = 0$.

The control parameters, in addition to the frequency, are also the length of the converter arm l_e, which has a significant impact on the dynamics of the system under examination. In the system, given the Lyapunov coefficients, in addition to zero initial conditions, a specific difference was assumed between the trajectories in the phase space, and its value was assumed as $\epsilon(0) = 10^{-5}$ [65]. To generate the map shown in Figure 9, 250×10^3 simulations had to be performed, which is very time-consuming from the numerical point of view and allows obtaining an image of 500×500 points.

The values of the coefficient λ presented in Figure 9 define specific solutions, where positive values of λ refer to the chaotic dynamic response of the system and where their negative values, $\lambda < 0$, mean the system response as periodic with appropriate phase trajectories heading to stable points or periodic orbits, which is presented below. When λ approaches zero, we are dealing with the so-called bifurcation points (or quasiperiodic solutions—bifurcation). As presented in Figure 9, in the low-frequency range (lifting speed multiplied by the i_{wh} ratio), the chaotic zone occurs almost exclusively for the arm length in the range of 0.1 to 0.15 m. The widest chaotic zone is observed in the range of medium and high excitation frequencies in the entire range of arm length l_e. Because the RMS value of the voltage generated on the piezoelectric electrodes was chosen as the indicator of the efficiency of energy acquisition from the M-EHS, the discussed map of the maximum Lyapunov exponents was compared with the diagrams of the RMS voltage in the entire excitation frequency range. As can be seen in Figure 10, for selected values of the l_e (0.07, 0.035, 0.01), both chaotic zones and zones of periodic solutions, and the corresponding RMS voltage values, can be clearly defined.

The determined value of U_{rms} (RMS: root mean square) of the voltage has been compared with the value of the excitation frequency ω. For the value $l_e = 0.01$ m, the bifurcation diagram (Figure 10) and the corresponding changes in the RMS value of the voltage are presented. In a range from c_1 to c_2 and c_3 to c_4 (Figures 9 and 10), there are two chaotic zones for which the values of the generated RMS voltage reach values in the range of 6–10 V. The M-EHS is characterized by high efficiency in the range of medium and high-frequency excitation reaching the value of 15 V for $\omega = 30$ s^{-1}.

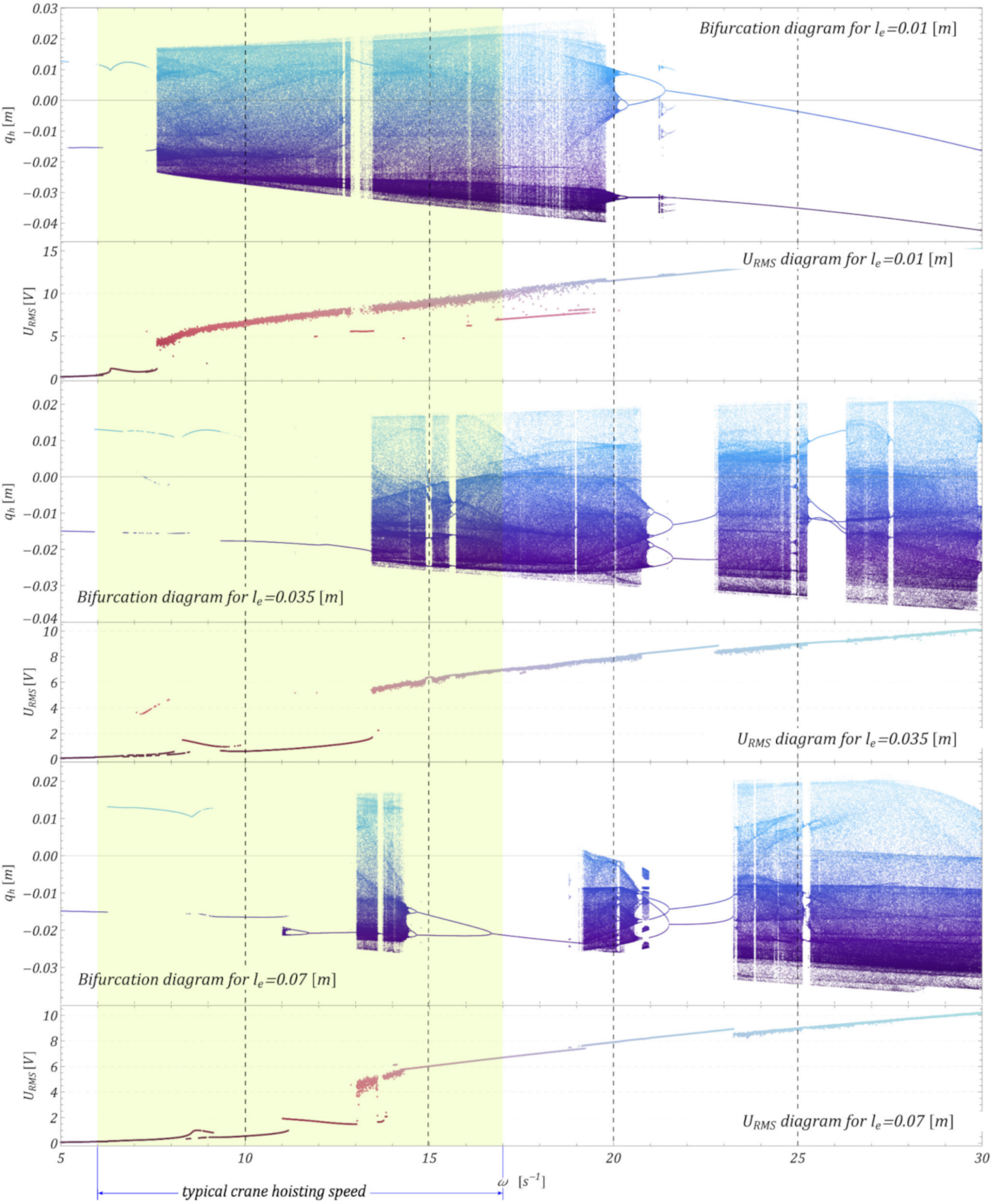

Figure 10. Examples of computer simulation results plotted against selected values of the arm length and frequency of excitation affecting the energy-harvesting system (bifurcation diagram, RMS voltage diagram).

Subsequently, for $l_e = 0.035$ and 0.07 m, a decrease in efficiency is observed, which is related to the specificity of the operation of the motion converter (decrease in speed $\dot{q}_e$). For points b_1–b_2 and b_3–b_4, respectively, there are wide chaotic zones, similarly for the range from point b_5 to the end of the range of the tested excitation frequency. In the range b_2–b_3, a bifurcation in the form of the multiplication of periodicity can be observed, as it can in the range b_4–b_5. The least effective system works for $l_e = 0.07$ m, where for low and medium excitation frequencies, the effective voltage reaches only a few volts (0–4). As in the previous case, there are four chaotic zones, but in a narrower frequency band. The discussed chaotic zones and zones of periodic solutions are presented below in the form of time diagrams and in the form of attractors allowed to present chaotic regions. Classically, to obtain the geometric shape of the attractor, visualization in the form of a Poincaré section was used.

To identify attractors, the value of the fractal dimension is widely used; however, the purpose of this study is not to conduct an in-depth analysis of the behavior of the system, only its effectiveness, which is why it was limited only to the presentation of selected cross sections on the two-dimensional phase plane, intending to show both multiperiod and chaotic solutions.

Figure 11 presents an exemplary one $\left(\omega_w = 1.3\ \mathrm{s}^{-1}\right)$ and two-period solutions $\omega_w = 0.735\ \mathrm{s}^{-1}$ for $l_e = 0.01$ m and the corresponding time series (Figure 12) of beam end vibrations and the voltage generated on piezoelectric electrodes. In this case, the time series of voltage changes are characterized by high repeatability, which results in significant efficiency for the RMS values. Figure 13 presents two chaotic solutions that perfectly reflect the Poincaré sections for $\omega_w = 0.8\ \mathrm{s}^{-1}$ and $1.47\ \mathrm{s}^{-1}$, i.e., for the excitation value corresponding to the considered hoisting mechanism of the tested crane. Thus, it turns out that for the arm length of 0.01 and the speed of $0.2\ \mathrm{ms}^{-1}$, the system generates an effective voltage in the range of approximately 8 V. Accordingly, for the attractors presented in Figure 14, the time series of the beam vibrations and voltage, as the well as phase trajectories for chaotic solutions, are listed. Reflecting the least effective solution, i.e., for an arm $l_e = 0.07$ m, Figure 15 presents two-period solutions $\left(\omega_w = 1.47\ \mathrm{s}^{-1}\right)$ and four-period solutions for $\left(\omega_w = 2.116\ \mathrm{s}^{-1}\right)$, which can also be observed in the bifurcation diagram (Figure 10) for specific values of ω_w. For the selected multiperiod solutions, the voltage-time series and the amplitude of the M-EHS beam end vibrations were also compared (Figure 16). For $l_e = 0.07$, there are also chaotic solutions presented (Figure 17), for $\omega_w = 1.325\ \mathrm{s}^{-1}$ and for $\omega_w = 2.357\ \mathrm{s}^{-1}$. In Figures 17 and 18, the corresponding phase trajectories and the time series of the voltage on the piezoelectric electrodes and the amplitude of the beam vibrations are shown.

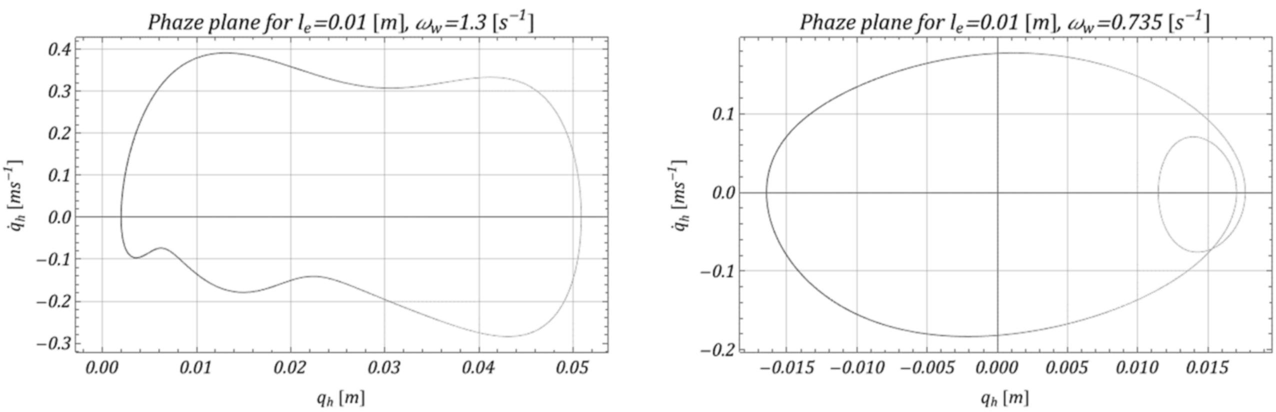

Figure 11. Phase diagrams related to selected solutions—periodic solutions for l_e = 0.01 m.

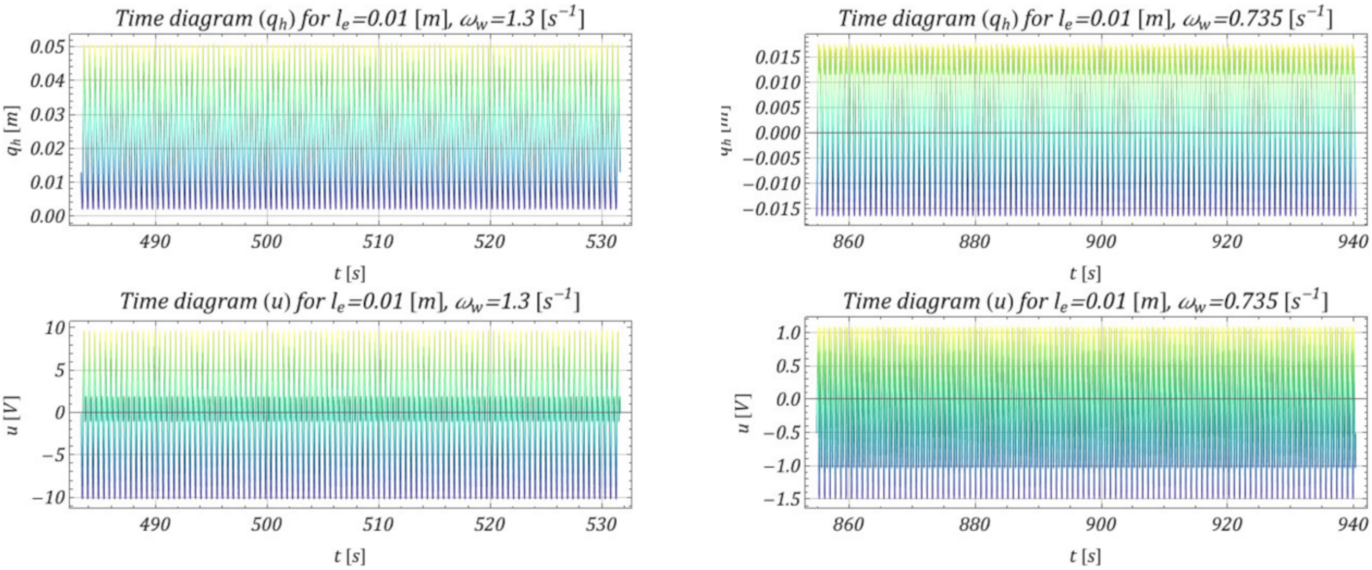

Figure 12. Voltage output and displacement time series related to selected solutions—sample periodic solutions for l_e = 0.01 m.

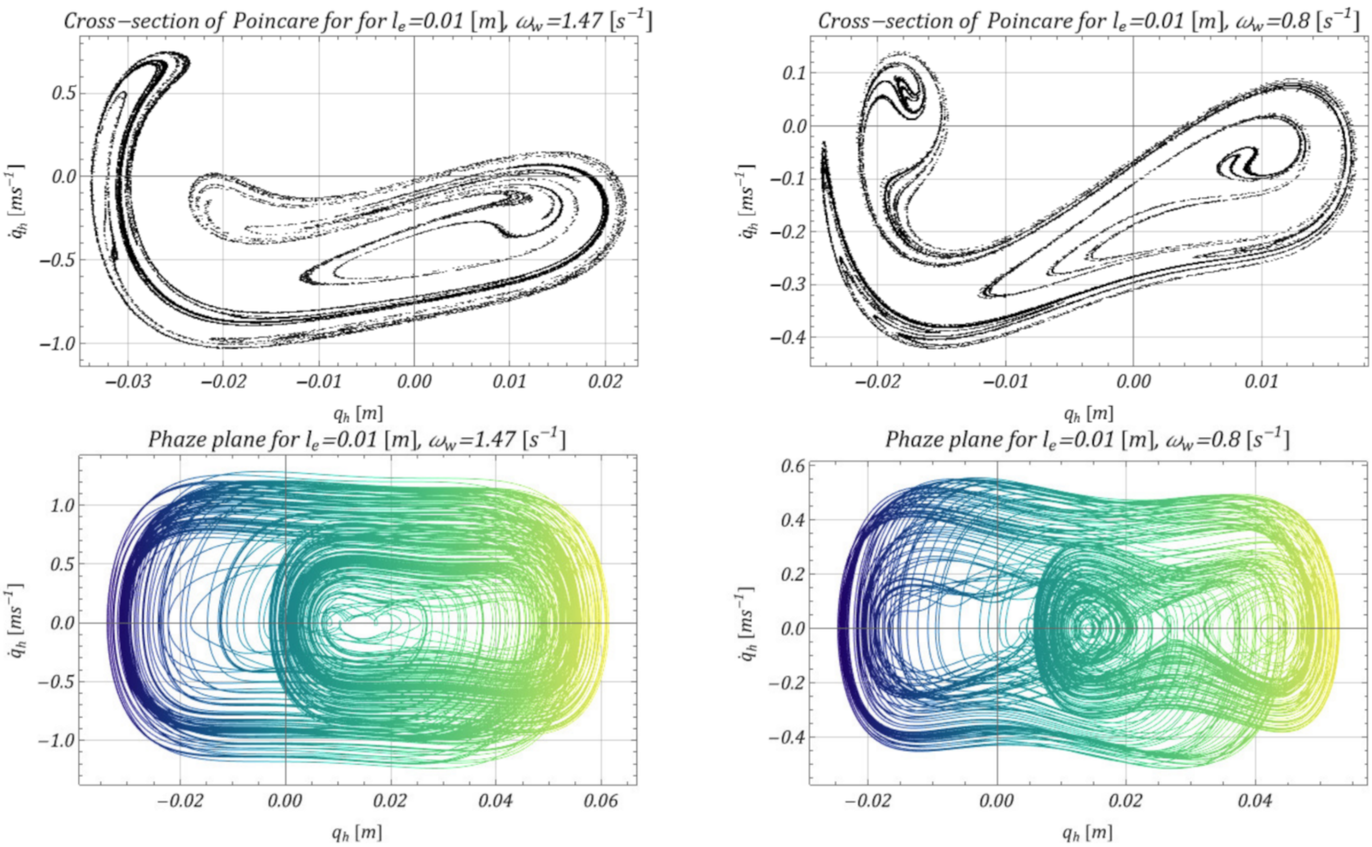

Figure 13. Phase diagrams and Poincaré maps related to selected solutions—sample chaotic solutions for l_e = 0.01 m.

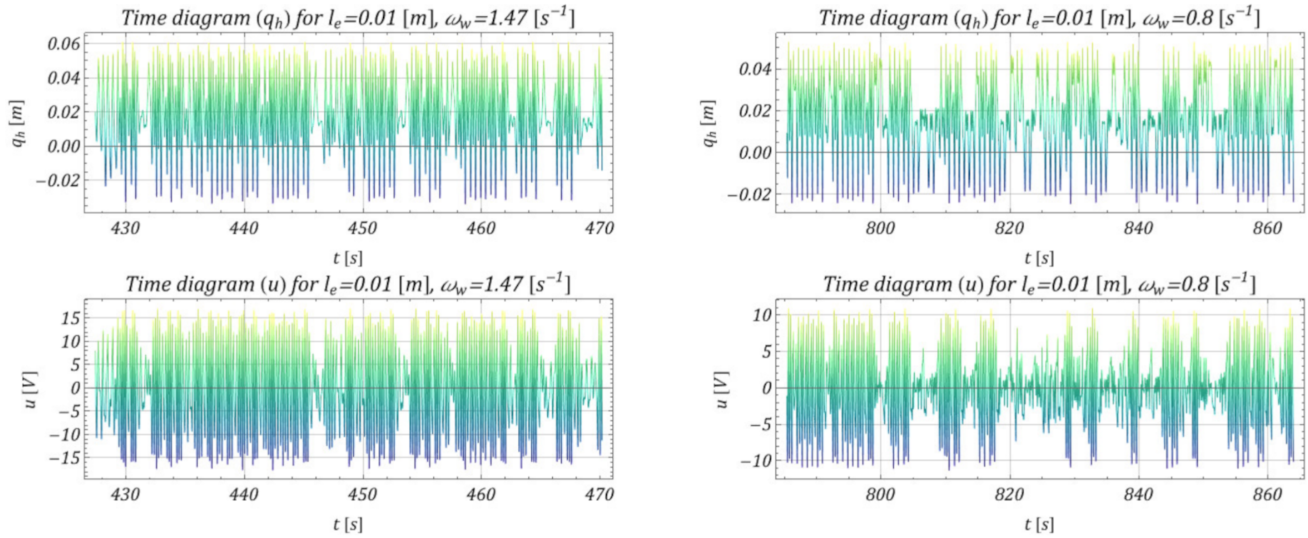

Figure 14. Voltage output and displacement time series related to selected solutions—sample chaotic solutions for l_e = 0.01 m.

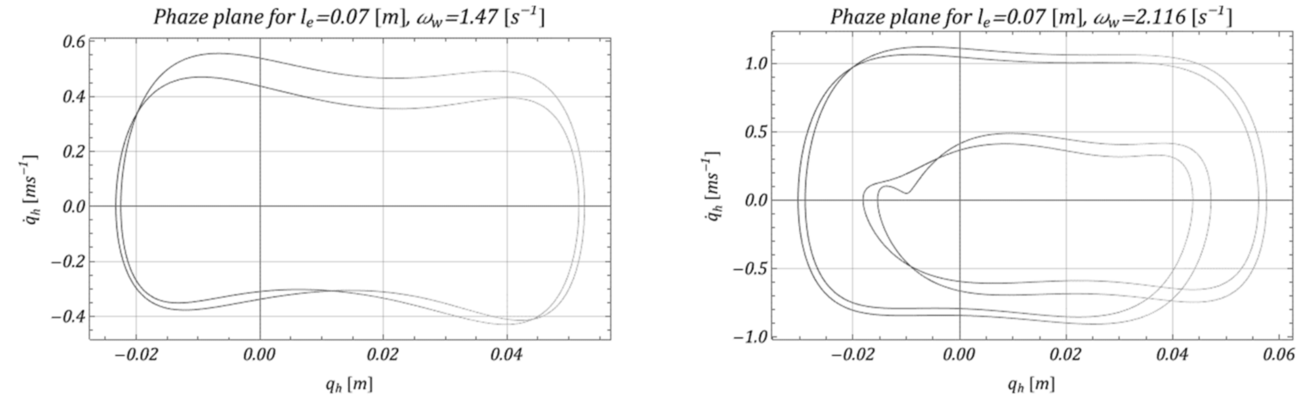

Figure 15. Phase diagrams related to selected solutions—periodic solutions for l_e = 0.07 m.

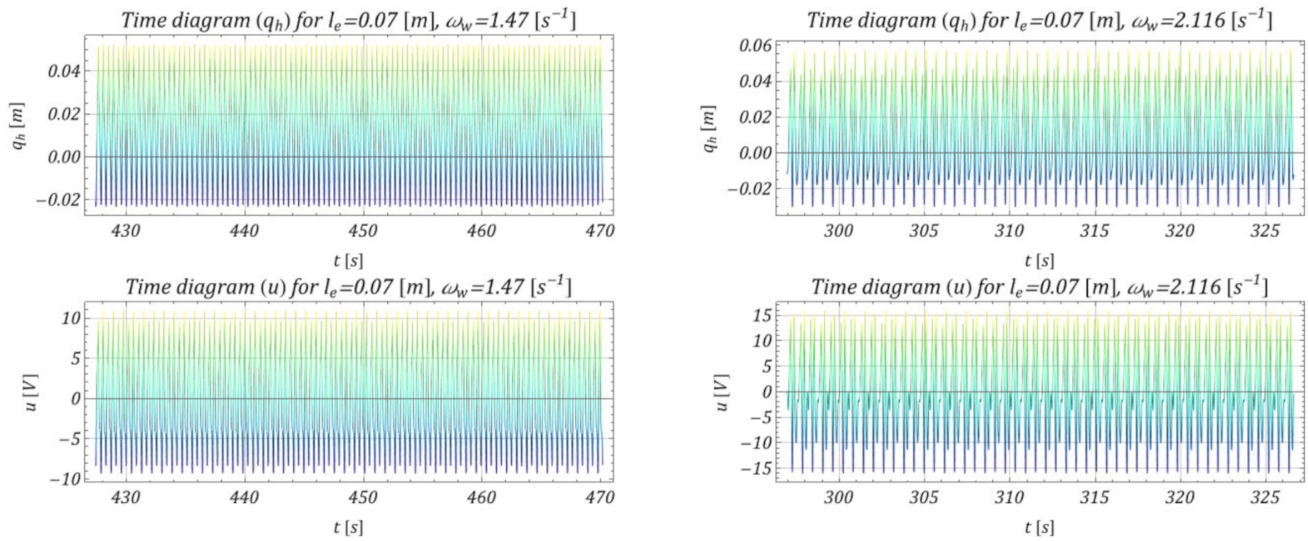

Figure 16. Voltage output and displacement time series related to selected solutions—sample periodic solutions for l_e = 0.07 m.

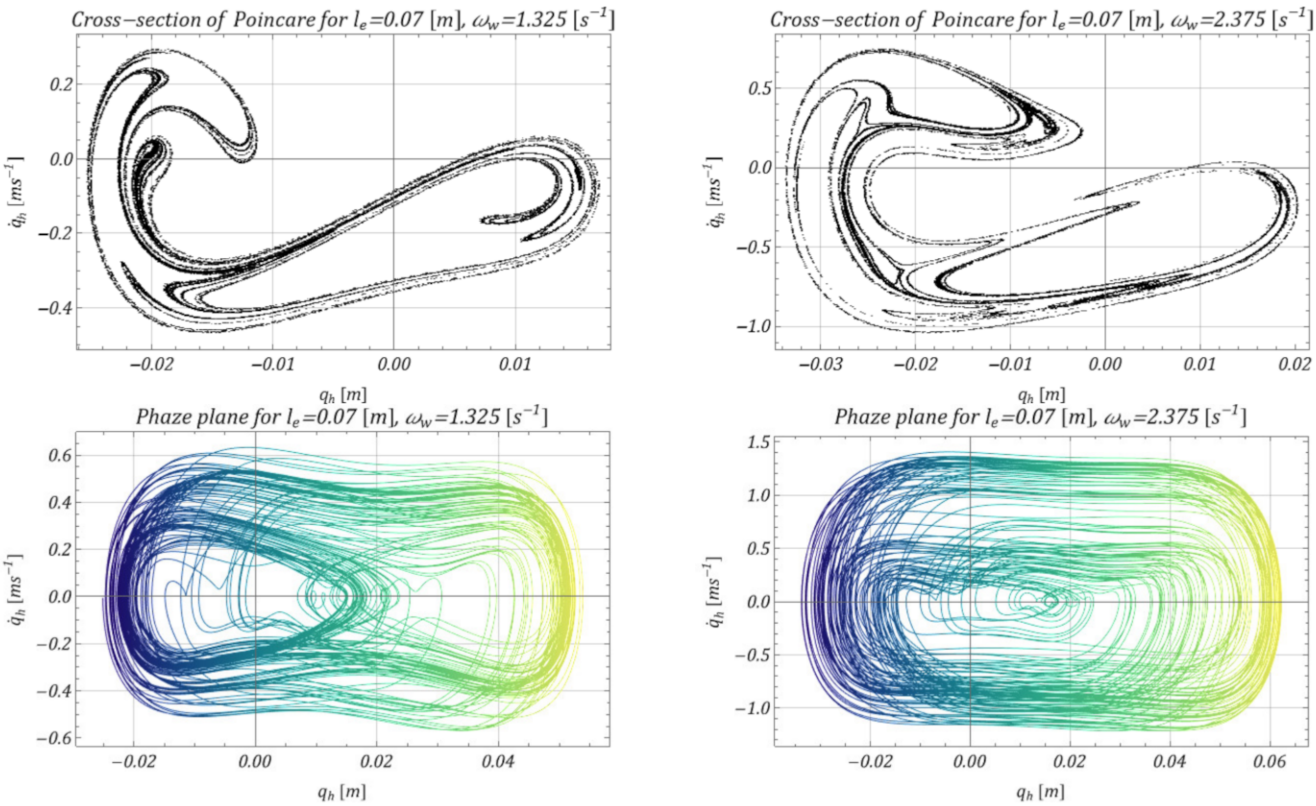

Figure 17. Phase diagrams and Poincaré maps related to selected solutions—Sample chaotic solutions for l_e = 0.07 m.

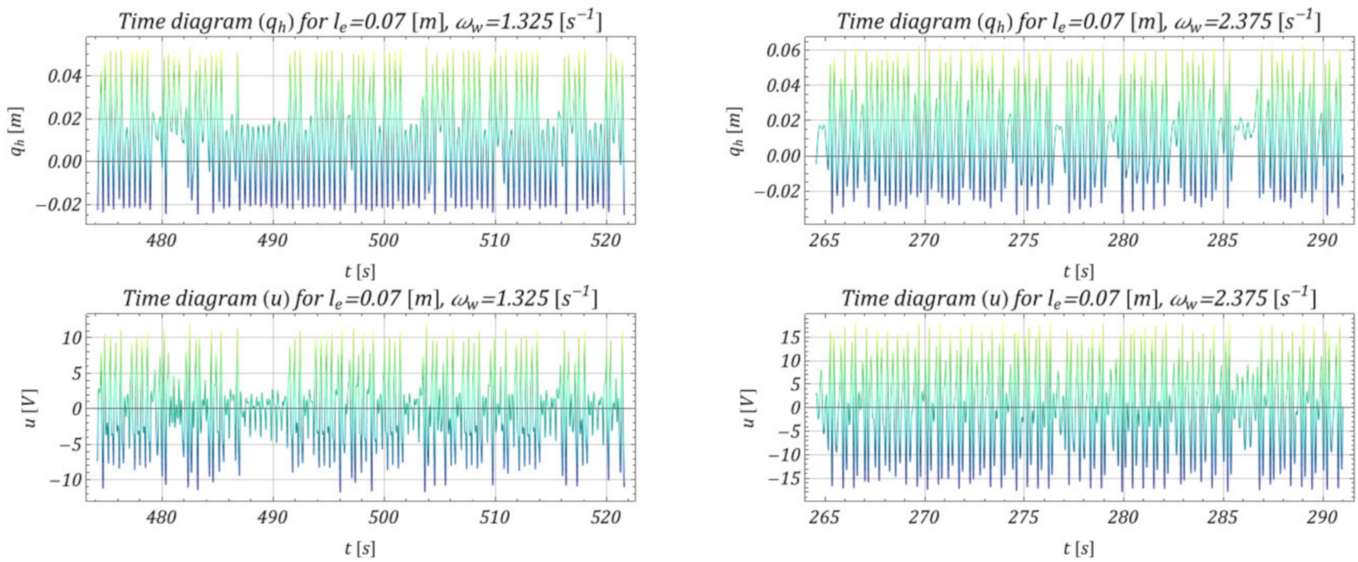

Figure 18. Voltage output and displacement time series related to selected solutions—sample chaotic solutions for l_e = 0.07 m.

5. Summary and Conclusions

The paper presented a complex dynamics analysis process of a new solution of the M-EHS system to be used on the hoisting mechanism of any crane. The article focused on the efficiency of energy harvesting in selected configuration cases. All numerical considerations were based on zero initial conditions. On the basis of the obtained results, the following conclusions can be drawn:

- The proposed M-EHS, together with the model of the hoisting mechanism, provided the possibility of analyzing any hoisting system together with the energy-harvesting system.
- The proposed mechanism of obtaining energy from the movement of the lower pulley was effective in a relatively wide range of operating speeds, which is shown in Figure 10 (range $\omega = 6$–$15\ s^{-1}$); because of the specific parameters of the vibrating system, relatively effective acquisition occurred for the working speed of the selected hoisting mechanism.
- Changing the parameters of the model, such as the excitation frequency and mainly the length of the l_e arm, made it possible to increase or decrease the efficiency, which can be seen in Figure 19, summarizing the values of the RMS voltage on the piezoelectric electrodes in selected ranges of the excitation frequency and the length of the l_e arm.

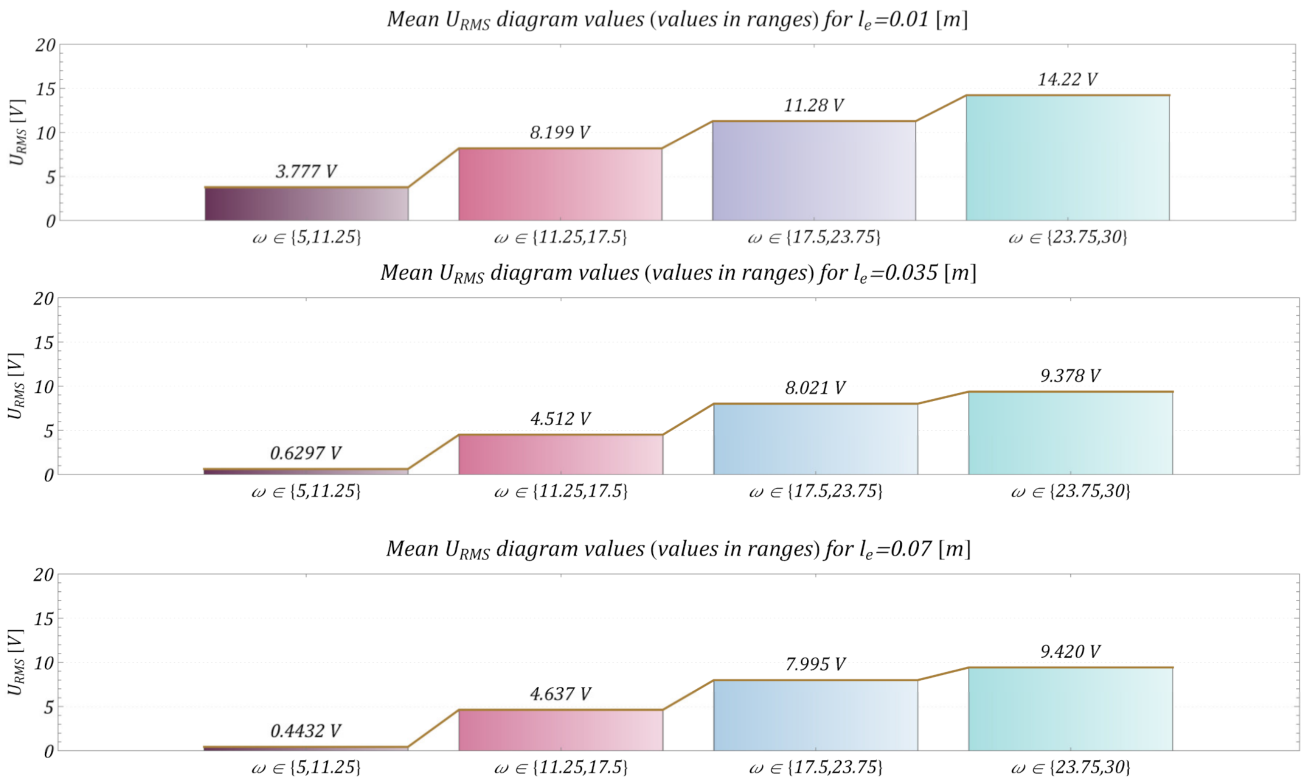

Figure 19. RMS voltage output related to selected bounds of angular velocity for selected l_e value.

The proposed model approach made it possible to maximize the recovery of energy that can be harvested during the operation of the hoisting mechanism, both during the period of unsteady operation and in the full range of steady operation related to the movement of the load to a given height.

The paper presented two phenomenological models that capture the dependencies that reflect the work of the crane-hoisting mechanism itself and the M-EHS model. On the basis of the model simulation, the signals that simulate the operation of the M-EHS were determined, and the time diagrams of the vibrations of the lower pulley axis and its course of changes in the angular velocity and angle of rotation over time for selected initial conditions and the condition of the rope were presented. The second stage included independent simulations for the selected excitation signals and simulations for a wider spectrum of rotational speeds, as well as the amplitude and frequency of vibrations for the M-EHS. The result was a list of voltage-time diagrams and bifurcation diagrams or RMS voltage for hoisting operating speed ranges and specific additional variables that affected the efficiency of energy acquisition, such as changing the length of the converter arm l_e.

Author Contributions: Conceptualization, T.H. and M.C.; methodology, T.H.; software, T.H.; validation, T.H. and M.C.; formal analysis, T.H. and M.C.; investigation, T.H. and M.C.; writing—original draft preparation, T.H. and M.C.; writing—review and editing, T.H. and M.C.; visualization, T.H. All authors have read and agreed to the published version of the manuscript.

Funding: This research received no external funding.

Data Availability Statement: Not applicable.

Acknowledgments: The authors thank the reviewers for their profound and valuable comments, which have contributed to enhancing the standard of the paper and the authors' future research in this area.

Conflicts of Interest: The authors declare no conflict of interest.

Abbreviations

EH	Energy harvesting
IoT	Internet of Things
M-EHS	Motion energy–harvesting system

References

1. International Energy Agency. World Energy Model Stated Policies Scenario. 2019. Available online: https://www.iea.org/reports/world-energy-model/stated-policies-scenario (accessed on 14 October 2022).
2. Nikas, A.; Gambhir, A.; Trutnevyte, E.; Koasidis, K.; Lund, H.; Thellufsen, J.Z.; Mayer, D.; Zachmann, G.; Miguel, L.; Ferreras-Alonso, N.; et al. Perspective of comprehensive and comprehensible multi-model energy and climate science in Europe. *Energy* **2021**, *215*, 119153. [CrossRef]
3. Priya, S.; Inman, D.J. (Eds.) *Energy Harvesting Technologies*; Springer: New York, NY, USA, 2009; Volume 21, p. 2.
4. Siddique, A.R.M.; Mahmud, S.; Van Heyst, B. A comprehensive review on vibration based micro power generators using electromagnetic and piezoelectric transducer mechanisms. *Energy Convers. Manag.* **2015**, *106*, 728–747. [CrossRef]
5. Akinaga, H. Recent advances and future prospects in energy harvesting technologies. *Jpn. J. Appl. Phys.* **2020**, *59*, 110201. [CrossRef]
6. Zhou, M.; Al-Furjan, M.S.H.; Zou, J.; Liu, W. A review on heat and mechanical energy harvesting from human–Principles, prototypes, and perspectives. *Renew. Sustain. Energy Rev.* **2018**, *82*, 3582–3609. [CrossRef]
7. Fan, K.; Cai, M.; Wang, F.; Tang, L.; Liang, J.; Wu, Y.; Tan, Q. A string-suspended and driven rotor for efficient ultra-low frequency mechanical energy harvesting. *Energy Convers. Manag.* **2019**, *198*, 111820. [CrossRef]
8. Hamlehdar, M.; Kasaeian, A.; Safaei, M.R. Energy harvesting from fluid flow using piezoelectrics: A critical review. *Renew. Energy* **2019**, *143*, 1826–1838. [CrossRef]
9. Zou, H.X.; Li, M.; Zhao, L.C.; Gao, Q.H.; Wei, K.X.; Zuo, L.; Qian, F.; Zhang, W.M. A magnetically coupled bistable piezoelectric harvester for underwater energy harvesting. *Energy* **2021**, *217*, 119429. [CrossRef]
10. Khazaee, M.; Rezaniakolaie, A.; Moosavian, A.; Rosendahl, L. A novel method for autonomous remote condition monitoring of rotating machines using piezoelectric energy harvesting approach. *Sens. Actuators A Phys.* **2019**, *295*, 37–50. [CrossRef]
11. Fu, H.; Mei, X.; Yurchenko, D.; Zhou, S.; Theodossiades, S.; Nakano, K.; Yeatman, E.M. Rotational energy harvesting for self-powered sensing. *Joule* **2021**, *5*, 1074–1118. [CrossRef]
12. Dudem, B.; Kim, D.H.; Bharat, L.K.; Yu, J.S. Highly-flexible piezoelectric nanogenerators with silver nanowires and barium titanate embedded composite films for mechanical energy harvesting. *Appl. Energy* **2018**, *230*, 865–874. [CrossRef]
13. Abdelkareem, M.A.; Xu, L.; Ali, M.K.A.; Elagouz, A.; Mi, J.; Guo, S.; Liu, Y.; Zuo, L. Vibration energy harvesting in automotive suspension system: A detailed review. *Appl. Energy* **2018**, *229*, 672–699. [CrossRef]
14. Guo, T.; Liu, G.; Pang, Y.; Wu, B.; Xi, F.; Zhao, J.; Bu, T.; Fu, X.; Li, X.; Zhang, C.; et al. Compressible hexagonal-structured triboelectric nanogenerators for harvesting tire rotation energy. *Extrem. Mech. Lett.* **2018**, *18*, 1–8. [CrossRef]
15. Maurya, D.; Kumar, P.; Khaleghian, S.; Sriramdas, R.; Kang, M.G.; Kishore, R.A.; Kumar, V.; Song, H.-C.; Park, J.-M.; Taheri, S.; et al. Energy harvesting and strain sensing in smart tire for next generation autonomous vehicles. *Appl. Energy* **2018**, *232*, 312–322. [CrossRef]
16. Bosso, N.; Magelli, M.; Zampieri, N. Application of low-power energy harvesting solutions in the railway field: A review. *Veh. Syst. Dyn.* **2021**, *59*, 841–871. [CrossRef]
17. Zhang, X.; Pan, H.; Qi, L.; Zhang, Z.; Yuan, Y.; Liu, Y. A renewable energy harvesting system using a mechanical vibration rectifier (MVR) for railroads. *Appl. Energy* **2017**, *204*, 1535–1543. [CrossRef]
18. Zhang, X.; Zhang, Z.; Pan, H.; Salman, W.; Yuan, Y.; Liu, Y. A portable high-efficiency electromagnetic energy harvesting system using supercapacitors for renewable energy applications in railroads. *Energy Convers. Manag.* **2016**, *118*, 287–294. [CrossRef]

19. Song, Y. Finite-element implementation of piezoelectric energy harvesting system from vibrations of railway bridge. *J. Energy Eng.* **2019**, *145*, 04018076. [CrossRef]
20. Dalala, Z.; Alwahsh, T.; Saadeh, O. Energy recovery control in elevators with automatic rescue application. *J. Energy Storage* **2021**, *43*, 103168. [CrossRef]
21. Ahamad, N.B.B.; Su, C.L.; Zhaoxia, X.; Vasquez, J.C.; Guerrero, J.M.; Liao, C.H. Energy harvesting from harbor cranes with flywheel energy storage systems. *IEEE Trans. Ind. Appl.* **2019**, *55*, 3354–3364. [CrossRef]
22. Tan, K.H.; Fah, Y.F. Reducing fuel consumption using flywheel battery technology for rubber tyred gantry cranes in container terminals. *J. Power Energy Eng.* **2017**, *5*, 15–33. [CrossRef]
23. Wang, H.; Zhang, Q.; Xie, F. Dynamic tension test and intelligent coordinated control system of a heavy scraper conveyor. *IET Sci. Meas. Technol.* **2017**, *11*, 871–877. [CrossRef]
24. Iqbal, M.; Nauman, M.M.; Khan, F.U.; Abas, P.E.; Cheok, Q.; Iqbal, A.; Aissa, B. Vibration-based piezoelectric, electromagnetic, and hybrid energy harvesters for microsystems applications: A contributed review. *Int. J. Energy Res.* **2021**, *45*, 65–102. [CrossRef]
25. Miao, G.; Fang, S.; Wang, S.; Zhou, S. A low-frequency rotational electromagnetic energy harvester using a magnetic plucking mechanism. *Appl. Energy* **2022**, *305*, 117838. [CrossRef]
26. Li, Z.; Liu, Y.; Yin, P.; Peng, Y.; Luo, J.; Xie, S.; Pu, H. Constituting abrupt magnetic flux density change for power density improvement in electromagnetic energy harvesting. *Int. J. Mech. Sci.* **2021**, *198*, 106363. [CrossRef]
27. Deng, Z.; Dapino, M.J. Review of magnetostrictive vibration energy harvesters. *Smart Mater. Struct.* **2017**, *26*, 103001. [CrossRef]
28. Khan, F.U.; Qadir, M.U. State-of-the-art in vibration-based electrostatic energy harvesting. *J. Micromechan. Microeng.* **2016**, *26*, 103001. [CrossRef]
29. Zhang, Y.; Wang, T.; Luo, A.; Hu, Y.; Li, X.; Wang, F. Micro electrostatic energy harvester with both broad bandwidth and high normalized power density. *Appl. Energy* **2018**, *212*, 362–371. [CrossRef]
30. Erturk, A.; Inman, D.J. *Piezoelectric Energy Harvesting*; John Wiley & Sons: Hoboken, NJ, USA, 2011.
31. Sezer, N.; Koç, M. A comprehensive review on the state-of-the-art of piezoelectric energy harvesting. *Nano Energy* **2021**, *80*, 105567. [CrossRef]
32. Covaci, C.; Gontean, A. Piezoelectric energy harvesting solutions: A review. *Sensors* **2020**, *20*, 3512. [CrossRef]
33. Febbo, M.; Machado, S.P.; Osinaga, S.M. A novel up-converting mechanism based on double impact for non-linear piezoelectric energy harvesting. *J. Phys. D Appl. Phys.* **2020**, *53*, 475501. [CrossRef]
34. Vijayan, K.; Friswell, M.I.; Khodaparast, H.H.; Adhikari, S. Non-linear energy harvesting from coupled impacting beams. *Int. J. Mech. Sci.* **2015**, *96*, 101–109. [CrossRef]
35. Gibus, D.; Gasnier, P.; Morel, A.; Garraud, N.; Badel, A. Non-linear losses study in strongly coupled piezoelectric device for broadband energy harvesting. *Mech. Syst. Signal Process.* **2022**, *165*, 108370. [CrossRef]
36. Litak, G.; Margielewicz, J.; Gąska, D.; Wolszczak, P.; Zhou, S. Multiple solutions of the tristable energy harvester. *Energies* **2021**, *14*, 1284. [CrossRef]
37. Halim, M.A.; Park, J.Y. Modeling and experiment of a handy motion driven, frequency up-converting electromagnetic energy harvester using transverse impact by spherical ball. *Sens. Actuators A Phys.* **2015**, *229*, 50–58. [CrossRef]
38. Ramezanpour, R.; Nahvi, H.; Ziaei-Rad, S. Electromechanical behavior of a pendulum-based piezoelectric frequency up-converting energy harvester. *J. Sound Vib.* **2016**, *370*, 280–305. [CrossRef]
39. Fu, H.; Yeatman, E.M. A methodology for low-speed broadband rotational energy harvesting using piezoelectric transduction and frequency up-conversion. *Energy* **2017**, *125*, 152–161. [CrossRef]
40. Izadgoshasb, I.; Lim, Y.Y.; Tang, L.; Padilla, R.V.; Tang, Z.S.; Sedighi, M. Improving efficiency of piezoelectric based energy harvesting from human motions using double pendulum system. *Energy Convers. Manag.* **2019**, *184*, 559–570. [CrossRef]
41. Kumar, R.; Gupta, S.; Ali, S.F. Energy harvesting from chaos in base excited double pendulum. *Mech. Syst. Signal Process.* **2019**, *124*, 49–64. [CrossRef]
42. Dell'Anna, F.; Dong, T.; Li, P.; Wen, Y.; Yang, Z.; Casu, M.R.; Azadmehr, M.; Berg, Y. State-of-the-art power management circuits for piezoelectric energy harvesters. *IEEE Circuits Syst. Mag.* **2018**, *18*, 27–48. [CrossRef]
43. Alghisi, D.; Ferrari, V.; Ferrari, M.; Crescini, D.; Touati, F.; Mnaouer, A.B. Single-and multi-source battery-less power management circuits for piezoelectric energy harvesting systems. *Sens. Actuators A Phys.* **2017**, *264*, 234–246. [CrossRef]
44. Lefeuvre, E.; Badel, A.; Brenes, A.; Seok, S.; Yoo, C.S. Power and frequency bandwidth improvement of piezoelectric energy harvesting devices using phase-shifted synchronous electric charge extraction interface circuit. *J. Intell. Mater. Syst. Struct.* **2017**, *28*, 2988–2995. [CrossRef]
45. Zhang, Z.; Xiang, H.; Shi, Z.; Zhan, J. Experimental investigation on piezoelectric energy harvesting from vehicle-bridge coupling vibration. *Energy Convers. Manag.* **2018**, *163*, 169–179. [CrossRef]
46. Keshmiri, A.; Deng, X.; Wu, N. New energy harvester with embedded piezoelectric stacks. *Compos. Part B Eng.* **2019**, *163*, 303–313. [CrossRef]
47. Wang, J.; Gu, S.; Zhang, C.; Hu, G.; Chen, G.; Yang, K.; Yurchenko, D. Hybrid wind energy scavenging by coupling vortex-induced vibrations and galloping. *Energy Convers. Manag.* **2020**, *213*, 112835. [CrossRef]
48. Lallart, M.; Zhou, S.; Yang, Z.; Yan, L.; Li, K.; Chen, Y. Coupling mechanical and electrical nonlinearities: The effect of synchronized discharging on tristable energy harvesters. *Appl. Energy* **2020**, *266*, 114516. [CrossRef]

49. Margielewicz, J.; Gąska, D.; Litak, G.; Wolszczak, P.; Trigona, C. Nonlinear Dynamics of a Star-Shaped Structure and Variable Configuration of Elastic Elements for Energy Harvesting Applications. *Sensors* **2022**, *22*, 2518. [CrossRef]
50. Margielewicz, J.; Gąska, D.; Litak, G.; Wolszczak, P.; Yurchenko, D. Nonlinear dynamics of a new energy harvesting system with quasi-zero stiffness. *Appl. Energy* **2022**, *307*, 118159. [CrossRef]
51. Li, X.; Zhang, J.; Li, R.; Dai, L.; Wang, W.; Yang, K. Dynamic responses of a two-degree-of-freedom bistable electromagnetic energy harvester under filtered band-limited stochastic excitation. *J. Sound Vib.* **2021**, *511*, 116334. [CrossRef]
52. Yang, K.; Tong, W.; Lin, L.; Yurchenko, D.; Wang, J. Active vibration isolation performance of the bistable nonlinear electromagnetic actuator with the elastic boundary. *J. Sound Vib.* **2022**, *520*, 116588. [CrossRef]
53. Li, X.; Yurchenko, D.; Li, R.; Feng, X.; Yan, B.; Yang, K. Performance and dynamics of a novel bistable vibration energy harvester with appended nonlinear elastic boundary. *Mech. Syst. Signal Process.* **2023**, *185*, 109787. [CrossRef]
54. Ahmad, M.M.; Khan, N.M.; Khan, F.U. Multi-degrees of freedom energy harvesting for broad-band vibration frequency range: A review. *Sens. Actuators A Phys.* **2022**, *344*, 113690. [CrossRef]
55. Gąska, D.; Margielewicz, J.; Haniszewski, T.; Matyja, T.; Konieczny, Ł.; Chróst, P. Numerical identification of the overhead travelling crane's dynamic factor caused by lifting the load off the ground. *J. Meas. Eng.* **2015**, *3*, 1–8.
56. Haniszewski, T. *Metodyka Modelowania Mechanizmów Wykonawczych Suwnic*; Politechniki Śląskiej: Polish Province of Silesia, Poland, 2021; p. 894.
57. Costello, G.A. *Theory of Wire Rope*; Springer: New York, NY, USA, 1997. [CrossRef]
58. Zhou, S.; Cao, J.; Erturk, A.; Lin, J. Enhanced Broadband Piezoelectric Energy Harvesting Using Rotatable Magnets. *Appl. Phys. Lett.* **2013**, *102*, 173901. [CrossRef]
59. Zhang, X.; Yang, W.; Zuo, M.; Tan, H.; Fan, H.; Mao, Q.; Wan, X. An Arc-Shaped Piezoelectric Bistable Vibration Energy Harvester: Modeling and Experiments. *Sensors* **2018**, *18*, 4472. [CrossRef] [PubMed]
60. Stanton, S.C.; McGehee, C.C.; Mann, B.P. Nonlinear Dynamics for Broadband Energy Harvesting: Investigation of a Bistable Piezoelectric Inertial Generator. *Phys. D Nonlinear Phenom.* **2010**, *239*, 640–653. [CrossRef]
61. Zhou, S.; Cao, J.; Inman, D.J.; Lin, J.; Liu, S.; Wang, Z. Broadband Tristable Energy Harvester: Modeling and Experiment Verification. *Appl. Energy* **2014**, *133*, 33–39. [CrossRef]
62. Huang, D.; Zhou, S.; Litak, G. Theoretical Analysis of Multi-Stable Energy Harvesters with High-Order Stiffness Terms. *Commun. Nonlinear Sci. Numer. Simul.* **2019**, *69*, 270–286. [CrossRef]
63. Strogatz, S.H. *Nonlinear Dynamics and Chaos: With Applications to Physics, Biology, Chemistry, and Engineering*; CRC Press: Boca Raton, FL, USA, 2018. [CrossRef]
64. Upadhyay, R.K.; Iyengar, S.R.K. *Introduction to Mathematical Modeling and Chaotic Dynamics*; Chapman and Hall/CRC: New York, NY, USA, 2013; pp. 1–349.
65. Litak, G.; Margielewicz, J.; Gaska, D.; Rysak, A.; Trigona, C. On Theoretical and Numerical Aspects of Bifurcations and Hysteresis Effects in Kinetic Energy Harvesters. *Sensors* **2022**, *22*, 381. [CrossRef]